A&A, 713, A294 (2026)
https://doi.org/10.1051/0004-6361/202660897
© The Authors 2026

Astronomy & Astrophysics

Constraining the model-based uncertainties of asteroseismic magnetic field measurements in red giants

L. Buchele[1,⋆], L. Bugnet[1], N. Muntean[1], and E. Hatt[1,2]

[1] Institute of Science and Technology Austria, 3400 Klosterneuburg, Austria
[2] School of Physics & Astronomy, University of Birmingham, Edgbaston, Birmingham B15 2TT, UK

Received 12 May 2026 / Accepted 17 July 2026

ABSTRACT

Context. Magnetic fields in the radiative interiors of red giants are measured using shifts in the stellar oscillation frequencies. In the asymptotic framework, however, converting an observed frequency shift into a radial magnetic field strength requires knowing the global magnetic sensitivity. The parameter that describes this sensitivity (also called the core structure parameter) must be inferred from stellar models, which introduces a potential source of uncertainty.
Aims. We seek to understand how the global magnetic sensitivity depends on stellar properties such as mass and metallicity, and to quantify the model-based uncertainty on magnetic field measurements. We also explore the stellar properties that are key for a precise and accurate estimate of the global magnetic sensitivity parameter.
Methods. Using MESA models, we examined how the global magnetic sensitivity changes with mass, metallicity, and age. We then created a sample of synthetic stars and tested how well our grid-based fitting method recovered the sensitivity parameter. We considered different grid construction approaches and the choice of which observational properties are used in the fitting process.
Results. The global magnetic sensitivity depends more strongly on mass for higher-mass models and the metallicity dependence is stronger for lower-metallicity models. Our fitting methods recover the underlying sensitivity parameter well, with a model-based uncertainty of 10% when precise metallicity measurements were used. We applied our procedure to stars with existing magnetic field measurements. In most cases, the dominant source of uncertainty remains observational, although such precise modeling can significantly reduce the magnetic field uncertainty for stars with exceptional data.
Conclusions. With careful fitting, stellar models yield accurate values for the global magnetic sensitivity. We recommend that future work obtain the global magnetic sensitivity using asteroseismic and high-quality spectroscopic constraints. Under these conditions, we recommend adopting a model-based uncertainty of 10% on the sensitivity parameter.

Key words. asteroseismology – stars: evolution – stars: low-mass – stars: magnetic field

1. Introduction

High-quality space-based asteroseismic data provide avenues for exploring stellar physics for many different types of stars. The primary focus of this work are red giants. It has been known for some time that classic stellar evolution models (e.g., Cantiello et al. 2014; Ceillier et al. 2017; Eggenberger et al. 2022) do not reproduce the measured core and envelope rotation rates (Beck et al. 2012; Mosser et al. 2012b; Deheuvels et al. 2014; Di Mauro et al. 2016; Triana et al. 2017; Gehan et al. 2018; Li et al. 2024a). One of the proposed solutions to this problem is that magnetic fields transport angular momentum (Cantiello et al. 2014; Spada et al. 2016; Eggenberger et al. 2019; Fuller et al. 2019; Gouhier et al. 2022; Eggenberger et al. 2022; Moyano et al. 2023; Meduri et al. 2024). The efficiency of angular momentum transport provided by a magnetic field depends on the properties of the field (e.g., Takahashi & Langer 2021), and it therefore is a key part of addressing the angular momentum transport problem to ensure that measured field strengths are accurate. The high-quality asteroseismic data provided by the *Kepler* mission now enable us to measure the average radial magnetic field strengths in the radiative interiors of red giants (Li et al. 2022a; Deheuvels et al. 2023; Li et al. 2023a; Hatt et al. 2024; Villate et al. 2026) with the perturbative theory for weak to moderate magnetic fields (Bugnet et al. 2021; Mathis et al. 2021; Li et al. 2022a; Bugnet 2022; Mathis & Bugnet 2023; Bhattacharya et al. 2024; Das et al. 2024). In addition, the effect of stronger near-critical fields (Fuller et al. 2015; Loi 2020) can be studied using the traditional approximation of rotation and magnetism (TARM, Dhouib et al. 2022; Rui et al. 2024; Lignières et al. 2024; Deheuvels et al. 2026). In our study, we remain within the perturbative framework and consider the magnetic field strength small enough not to be affected by near-critical effects (see Bugnet et al. 2021, for validity criteria).

The rotational profiles (e.g., Beck et al. 2012) and these internal magnetic fields (e.g., Bugnet et al. 2021; Li et al. 2022a) can be measured by observing shifts in the oscillation mode frequencies. The average core rotation can directly be determined from these shifts (e.g., Beck et al. 2012; Mosser et al. 2012b; Gehan et al. 2018; Li et al. 2024a), or rotational inversions can be performed using a stellar reference model to obtain the core and envelope rotation rates (e.g., Deheuvels et al. 2014; Di Mauro et al. 2016; Ahlborn et al. 2022). In the case of magnetic fields, stellar models are also necessary to convert the measured magnetic splitting into average magnetic field strength (Mathis et al. 2021; Li et al. 2022a). While some work has been done to understand the uncertainty introduced by stellar modeling for rotational inversions (Ahlborn et al. 2025), less attention has been paid to the potential model dependence of magnetic field measurements. Bugnet et al. (2021) investigated

⋆ Corresponding author: lynn.buchele@ist.ac.at

Open Access article, published by EDP Sciences, under the terms of the Creative Commons Attribution License (https://creativecommons.org/licenses/by/4.0), which permits unrestricted use, distribution, and reproduction in any medium, provided the original work is properly cited.
This article is published in open access under the Subscribe to Open model. Subscribe to A&A to support open access publication.

the dependence of the magnetic signature on mass and metallicity before any observational magnetic signature had been detected. They showed that the stellar properties slightly affect the sensitivity of the modes to the magnetic fields. Now that a few dozen magnetic red giants are being characterized through the use of stellar models, it becomes important to estimate the modeling bias in the context of observational measurements.

The main method of measuring weak to moderate internal magnetic fields of red giants relies on measuring the g-mode frequency perturbation, $\delta\nu_{\rm mag}$, attributable to the magnetic field (Bugnet et al. 2021). In practice, it is common to take $\delta\nu_{\rm mag}$ as the magnetic shift for pure g modes at the frequency of maximum power, $\nu_{\rm max}$. The value of $\delta\nu_{\rm mag}$ is obtained from the observed mixed-dipole modes by fitting (Li et al. 2022a)

$$\delta\nu_{\rm mag,m=0} = \zeta\,(1-a)\delta\nu_{\rm mag}\left(\frac{\nu_{\rm max}}{\nu}\right)^3, \tag{1}$$

$$\delta\nu_{\rm mag,m=\pm1} = \zeta\left(1+\frac{a}{2}\right)\delta\nu_{\rm mag}\left(\frac{\nu_{\rm max}}{\nu}\right)^3, \tag{2}$$

where m is the azimuthal order, ζ is the gravity mode inertia, ν is the mode frequency, and a is a parameter that depends on the geometry of the field. In order to constrain $\delta\nu_{\rm mag}$ and a, all three components ($m = -1, 0, 1$) of the dipole modes must be visible. In Equations (1) and (2), ζ accounts for the fact that only the g part of the mixed mode is shifted by the magnetic field. Alternatively, the mixed mode can be decomposed into the underlying p and g components, and the magnetic shift can be directly applied to the g component, which is then recoupled to the pure p mode, as was done by Hatt et al. (2024). When an overall value of $\delta\nu_{\rm mag}$ has been obtained, this shift is then attributed to the dominant term of the magnetic field effect, which is the radial component of the field (Bugnet et al. 2021; Mathis et al. 2021; Li et al. 2022a). Li et al. (2022a), further expressed the asymptotic link between the average squared radial field strength and the magnetic shift as

$$\langle B_r^2\rangle = \frac{16\pi^4\mu_0}{\mathcal{I}}\nu_{\rm max}^3\delta\nu_{\rm mag}, \tag{3}$$

where μ_0 is the vacuum permeability, and $\mathcal{I}$ parameterizes the global magnetic sensitivity. In previous works (e.g., Li et al. 2022a), $\mathcal{I}$ was called the core structure parameter, but we refer to it as the global magnetic sensitivity to make its usage clearer. If the magnetic shift is calculated at an arbitrary frequency rather than $\nu_{\rm max}$, then this frequency replaces $\nu_{\rm max}$ in Equation (3). $\mathcal{I}$ is what allows us to convert the shift into a measured average field strength, and it is defined as

$$\mathcal{I} = \frac{\displaystyle\int_{r_i}^{r_o}\left(\frac{N}{r}\right)^3\frac{{\rm d}r}{\rho}}{\displaystyle\int_{r_i}^{r_o}\left(\frac{N}{r}\right){\rm d}r}, \tag{4}$$

where N is the buoyancy frequency (also called Brunt–Väisälä frequency), ρ is the density, and the integration bounds r_i and r_o are the inner and outer turning points of the g-mode cavity, respectively.

$\mathcal{I}$ cannot be directly observed and is therefore the only non-observational component leading to the estimate of the magnetic field strength in the perturbative framework (Li et al. 2022a, 2023a; Deheuvels et al. 2023; Hatt et al. 2024; Villate et al. 2026). Instead, it must be obtained from a stellar model, typically, the best-fit model to other observed stellar properties. Thus, there is some degree of dependence on the model used in the final estimate of the internal magnetic field strength from this simplified formulation. This dependence comes from the choices made when constructing the models and when finding the best-fit model.

Several works have used the method outlined above to measure internal magnetic fields in red giants, and each work has taken a different approach to quantifying the uncertainty introduced by inferring $\mathcal{I}$ from stellar models. Li et al. (2022a) used the $\mathcal{I}$ values of the models from their grid (which varied mass, metallicity, and age), which reproduced the large frequency separation ($\Delta\nu$) and the asymptotic period spacing of the dipole modes ($\Delta\Pi_1$). This method was also used by Deheuvels et al. (2023). Li et al. (2023a) also took the $\mathcal{I}$ value of the best-fitting model, although in this case, the model was fit to the stellar effective temperature ($T_{\rm eff}$), luminosity (L), metallicity ([Fe/H]), radial mode frequencies, and $\Delta\Pi_1$. For all but one star studied by Villate et al. (2026), $\mathcal{I}$ was obtained from the model that best fit the observed $\nu_{\rm max}$, $\Delta\nu$, and $\Delta\Pi_1$ values. The one exception was a star whose $\Delta\Pi_1$ value was below the $\Delta\nu$-$\Delta\Pi_1$ sequence expected from single-star evolution. In this case, Villate et al. (2026) found a best-fit model using the observed $\Delta\Pi_1$ alone. In all four works, the value of $\mathcal{I}$ has been taken from a best-fit model without including any model-based uncertainty.

In contrast, Hatt et al. (2024) included the uncertainty on $\mathcal{I}$ in the field strengths they reported. Their $\mathcal{I}$ values were found by fitting the observed $T_{\rm eff}$, [Fe/H], surface gravity, mass (M, obtained from scaling relations in Yu et al. 2018), $\Delta\Pi_1$, $\nu_{\rm max}$, $\Delta\nu$, and radial model frequencies. They found that the overall distribution of $\mathcal{I}$ from their best-fit models was approximated by a Gaussian with a width of 30% of the mean, and they therefore adopted a 30% uncertainty on $\mathcal{I}$.

These two approaches, assuming either no uncertainty on $\mathcal{I}$ or an uncertainty defined by the spread across all stars, represent the extremes of how model-based uncertainty can be accounted for. We aim to find a middle ground that acknowledges that while our stellar models likely do not fully represent the stars we observe, we still have some constraints on the properties of individual stars. To determine this middle ground, we seek to understand how the value of $\mathcal{I}$ depends on the choices made when constructing stellar models and the procedure used to find the best-fit model. To do this, we use two grids of models, described in Sect. 2. We focus on one grid of models to explore how $\mathcal{I}$ depends on the stellar parameters in Sect. 3. This provides us with some insight into what should be considered for an appropriate value of $\mathcal{I}$. In Sect. 4 we test how accurately known values of $\mathcal{I}$ are recovered using each grid of models and various sets of observational parameters. We then use our models and fitting procedure to infer $\mathcal{I}$ for red giant branch stars with previously measured average magnetic field strengths in Sect. 5. Finally, we present our conclusions and recommendations in Sect. 6.

2. Models

We used two different grids of stellar models generated using version `r24.08.1` of the Modules for Experiments in Stellar Astrophysics (MESA) stellar evolution code (Paxton et al. 2011, 2013, 2015, 2018, 2019; Jermyn et al. 2023). The parameters that were kept constant between the two grids are detailed in Appendix A. In general, our modeling choices followed those of Li & Joyce (2025), with the most significant change being that we used the exponential form of overshoot (Herwig 2000). Both grids covered the mass range $0.8\ {\rm M}_\odot \leq M \leq 1.8\ {\rm M}_\odot$ and initial metallicity range $-1 \leq [{\rm Fe/H}]_{\rm init} \leq 0.5$. In our grid labeled Linear, we adopted a linear sampling approach where

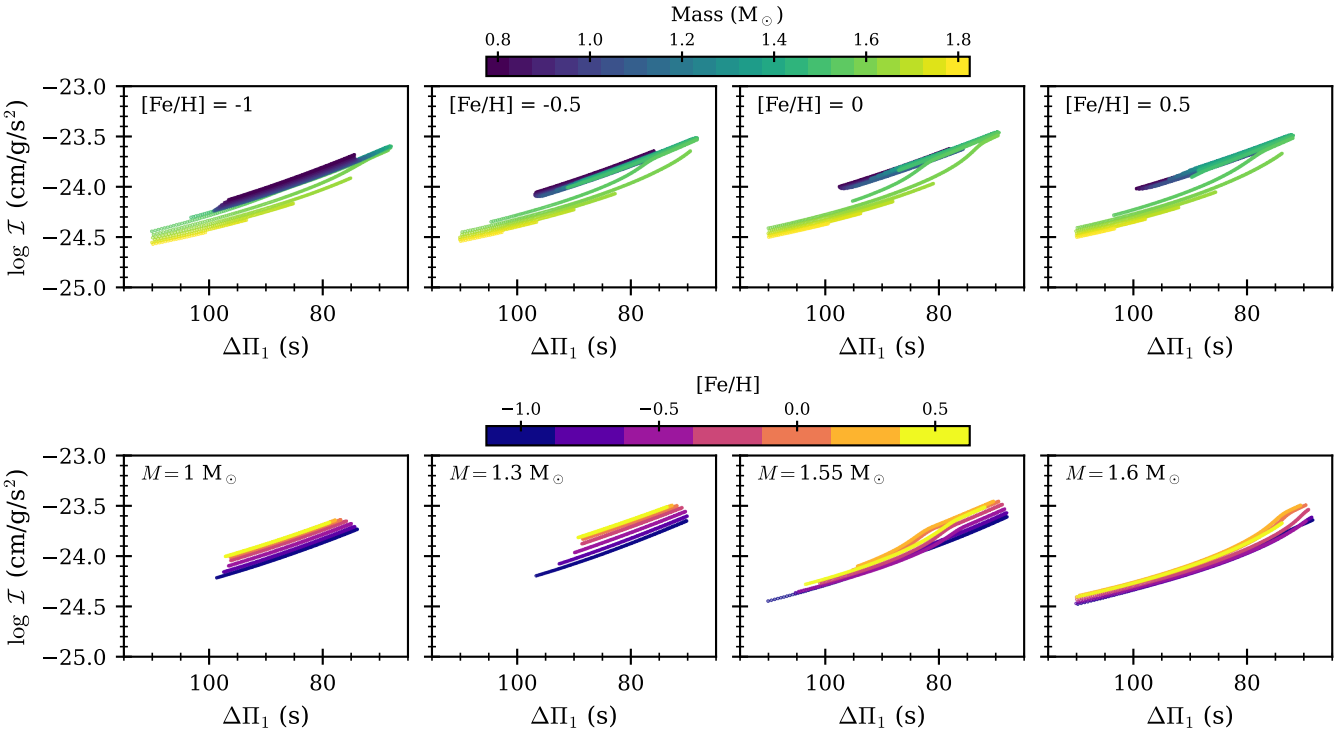


Fig. 1. Dependence of the global magnetic sensitivity, $\mathcal{I}$ (also called the core structure parameter), on stellar parameters for models in our linear grid. All panels show $\mathcal{I}$ as a function of $\Delta\Pi_1$ for a subset of tracks in our linear grid. In the top row, the tracks shown in each panel have the same metallicity, but vary in mass. In the bottom row, each panel shows tracks of the same mass, but different metallicity. In all panels, the $\Delta\Pi_1$-axis is reversed, such that a given evolutionary track evolves from left to right.

the models are evenly spaced in mass and initial metallicity with step sizes of 0.05 $M_\odot$ and 0.25 dex, respectively, leading to 147 tracks. In addition, the helium-enrichment law was fixed such that the initial helium mass fraction was $Y_{init} = 0.24 + 2Z_{init}$, where Z_{init} is the initial metal mass fraction. We also adopted a fixed mixing-length parameter ($\alpha_{mlt} = 2$) and fixed overshoot parameter ($f_{ov} = 0.015$). For our grid labeled Sobol, we adopted a quasi-random sampling of M, Y_{init}, $[Fe/H]_{init}$, α_{mlt}, and f_{ov} using a Sobol sequence (Sobol' 1967; see also Appendix B of Bellinger et al. 2016). We sampled the mass and metallicity in the same ranges as for our linear grid and used the following ranges for the additional free parameters: Yinit $\in [0.24, 0.33]$, $\alpha_{mlt} \in [1.3, 2.6]$, and $f_{ov} \in [0.004, 0.06]$. As this grid has three additional free parameters, we also increased the number of tracks to 2048 to ensure a sufficient sampling of the space.

We chose to use two grids for several reasons. First, although Sobol sequences provide better coverage of multidimensional parameter spaces, it is harder to isolate the effects of changing a single parameter because the quasi-random sampling returns stellar parameters that are always slightly different. This makes it more difficult to, for example, examine the difference between tracks of varying masses but fixed metallicity. We therefore use our linear grid to explore how $\mathcal{I}$ depends on the stellar parameters in Sect. 3. The second reason we used these two grids was to represent the modeling procedures used in previous works better. Although there are some differences in the physical prescriptions we used, the mass and metallicity values we chose in our Linear grid are the same as in the grid used by Hatt et al. (2024). Our Sobol grid was instead constructed to be closer to the grid used by Li et al. (2023a), which was initially described in Li et al. (2022b).

Along each track, we calculated $\Delta\nu$ using the radial mode frequencies obtained from the stellar oscillation code GYRE Townsend & Teitler (2013), $\Delta\Pi_1$ using the asymptotic form

$$\Delta\Pi_1 = \sqrt{2}\pi^2 \left(\int_{r_i}^{r_o} \frac{N}{r}\, \mathrm{d}r \right)^{-1}, \tag{5}$$

and $\mathcal{I}$ according to Equation (4). We provide more details about these calculations in Appendix A, including an important change from the MESA default calculation of $\Delta\Pi_1$. From each grid, we selected models with 100 μHz $\leq \nu_{max} \leq$ 277 μHz and $\Delta\Pi_1 < 110$ s, which roughly corresponds to the range of parameters in the sample of Hatt et al. (2024).

3. Dependence of $\mathcal{I}$ on stellar parameters

In order to explore how modeling choices can affect an inferred value of $\mathcal{I}$, it is first useful to understand how $\mathcal{I}$ depends on the stellar properties. To do this, we only used the models in our linear grid. In Fig. 1 we show the change in the evolution of $\mathcal{I}$ with varying mass and metallicity.

3.1. Effect of the mass

The dependence on mass (shown in the top row of the figure) clearly shows two regimes. The lower-mass models ($M \lesssim 1.55$ $M_\odot$) all lie along the same line, whereas the more massive models ($M \gtrsim 1.65$ $M_\odot$) show much lower values of $\mathcal{I}$ and a larger spread across different masses. Intermediate-mass models transition smoothly from the higher-mass (lower $\mathcal{I}$) regime to the lower-mass (higher $\mathcal{I}$) regime. As the metallicity is increased, the difference between the low- and high-mass

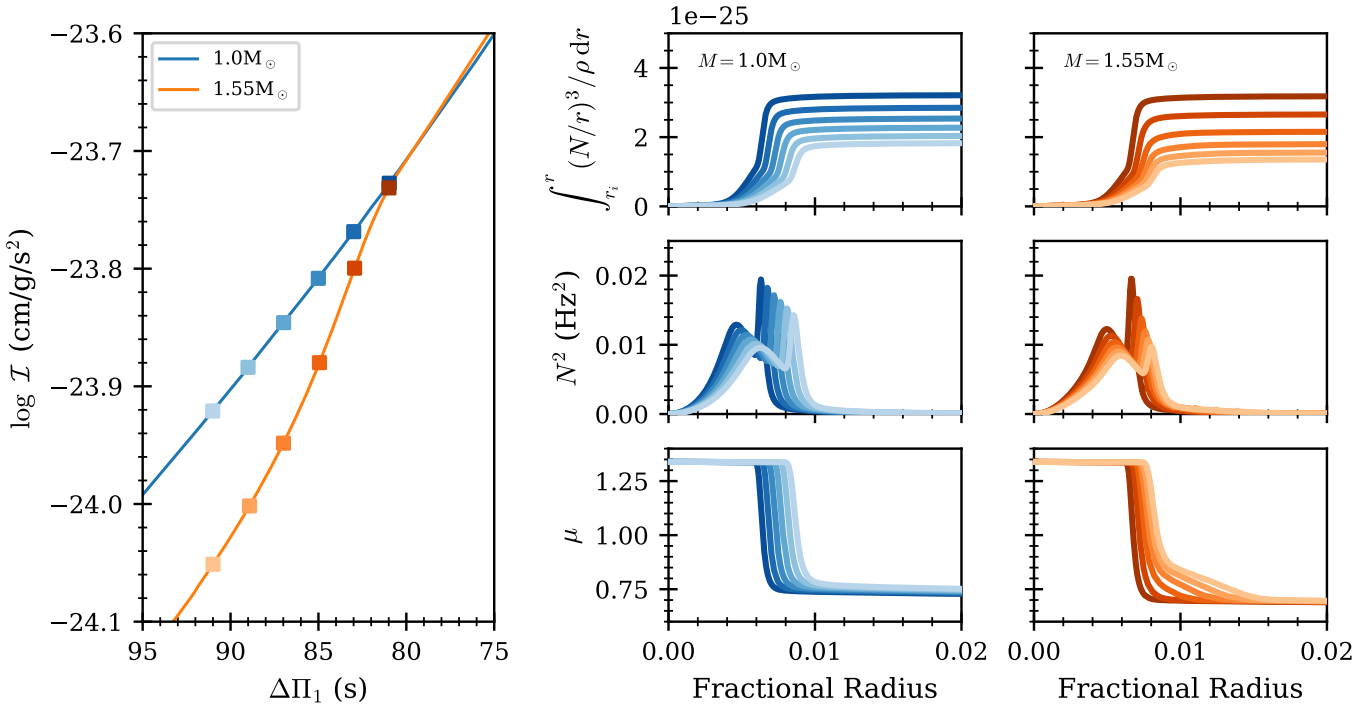


Fig. 2. Connection between mean molecular weight profiles and $\mathcal{I}$ for models with solar metallicity of two different masses. The leftmost panel shows the evolution of $\mathcal{I}$ for the two tracks, with squares indicating the selected models plotted in the second and third columns. The top panels in these columns show the cumulative integral of the numerator in Equation (4) for each selected model of each track. The middle and bottom panels in these two columns show the N^2 and μ profiles, respectively. In the second and third columns, the darker lines correspond to more evolved models. We note that although the burning shell moves outward in mass, the contraction of the core results in the burning shell moving inward in radius.

regimes increases. The bottom row of Fig. 1 shows that the $\mathcal{I}$ values in the lower-mass regime depend more strongly on the metallicity.

To explain this behavior, we return to the definition of $\mathcal{I}$ given in Equation (4). The denominator is proportional to $(\Delta\Pi_1)^{-1}$, and so we compare the structure of different models with similar $\Delta\Pi_1$ values. We focus in Fig. 2 on a small part of two evolutionary tracks with the same metallicity, but different masses. The integral in the numerator of Equation (4) is sensitive to the peak in N^2 caused by the chemical gradient in the hydrogen-burning shell. In the models along our lower-mass track in the $\Delta\Pi_1 - \mathcal{I}$ diagram, the hydrogen-burning shell has already passed through any gradients in the mean molecular weight (μ) created during the main-sequence evolution. Thus, the peak in N^2 increases because the hydrogen-burning shell narrows, which is caused by gravitational contraction. This further heats the degenerate core. In contrast, the higher-mass model enters our $\nu_{\max}$ regime before the burning shell has passed through the μ gradient left by the main-sequence evolution. Thus, as the star continues to evolve, the difference in μ above and below the burning shell increases rapidly as the burning shell moves into layers that experienced less main-sequence burning. This increasing μ gradient (shown in the bottom row of Fig. 2) causes max N^2 to increase rapidly until the burning shell reaches layers that were unaffected by fusion during the main sequence. From this point, the value of $\mathcal{I}$ evolves in the same manner as the lower-mass track. The precise moment along each track at which this transition occurs depends on the maximum extent of the convective core during the main sequence. This is the first hint that using different physics when modeling will yield different values of $\mathcal{I}$ because the extent of the convective core depends on the chosen treatment of convective boundary mixing.

It is important to note that several effects can reduce the number of stars with magnetic detections in the higher-mass lower-$\mathcal{I}$ regime. First, in the early part of the lower-$\mathcal{I}$ sequence, the stars are still settling onto the red giant branch, with cores that are not yet fully degenerate. This means that the stars are evolving on a Kelvin-Helmholtz timescale and can therefore be difficult to detect (Deheuvels et al. 2022). However, the final part of the transition from the lower-$\mathcal{I}$ sequence to the higher sequence occurs after the core is fully degenerate, and detections at this stage might therefore be more likely. In Appendix B we provide a plot showing the central electron degeneracy of several tracks to illustrate this point. Beyond the evolutionary timescales, magnetic signatures in stars with lower values of $\mathcal{I}$ are also inherently more difficult to detect. Equation (3) shows that for a given radial magnetic field strength and $\nu_{\max}$ value, lower values of $\mathcal{I}$ result in smaller (and therefore, more difficult to detect) magnetic splittings. This means that stars of higher masses require slightly stronger fields to be detectable this early in their evolution along the red giant branch. For example, the $\mathcal{I}$ value of a $1\,M_\odot$ star with $\Delta\Pi_1 = 90$ s is roughly twice as high as that of a $1.7\,M_\odot$ star with the same metallicity and $\Delta\Pi_1$ value. Thus, for the two stars to exhibit similar magnetic shifts, the average radial magnetic field in the $1.7\,M_\odot$ star needs to be $\sqrt{2}$ times higher than in the $1\,M_\odot$ star.

Despite these two effects, one star in the sample of Hatt et al. (2024) (KIC 10149324) lies above the degenerate sequence in the $\Delta\Pi_1 - \Delta\nu$ diagram, and therefore, might be in this rapid evolutionary phase. This motivated us to use observational parameters to obtain values of $\mathcal{I}$ from our grids of models instead of

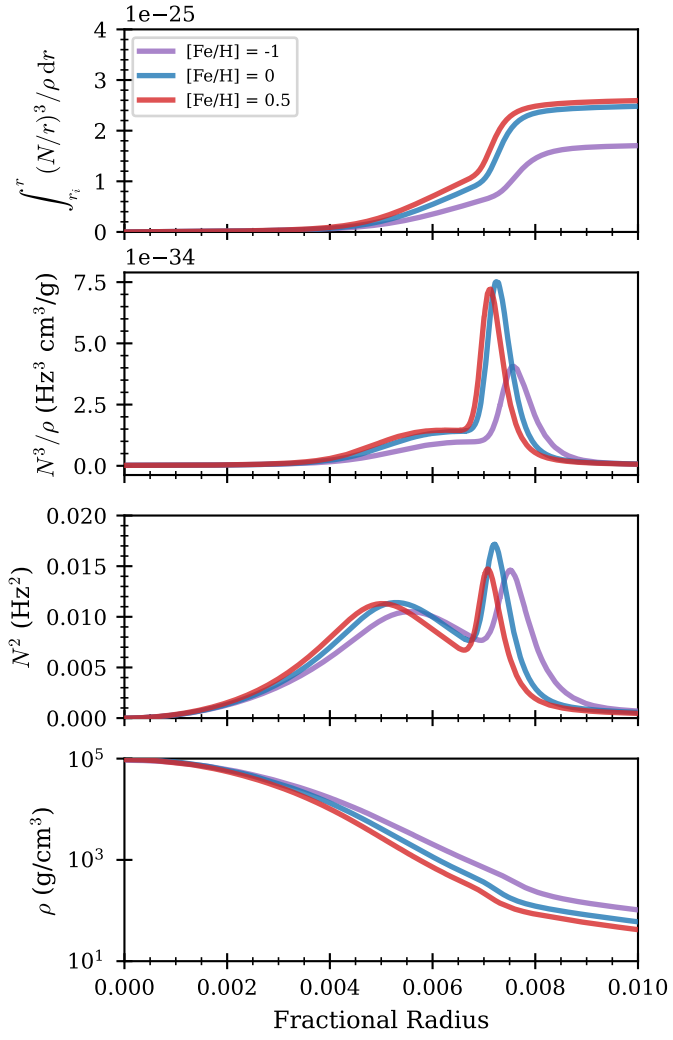


Fig. 3. Dependence of $\mathcal{I}$ on metallicity for three 1 $M_\odot$ models with the same $\Delta\Pi_1$. The top panel shows the cumulative integral of the numerator of Equation (4). The rightmost value of each line shows the value of $\mathcal{I}$ for each model. The second, third, and fourth panels show the N^3/ρ, N^2, and ρ profiles, respectively.

attempting to fit a relation between $\mathcal{I}$ and $\Delta\Pi_1$, as was done by Li et al. (2023a). This more general approach is even more important when magnetic signatures can be detected in very early higher-mass red giant branch stars.

3.2. Effect of the metallicity

When the hydrogen-burning shell has passed the μ gradient left behind by the main-sequence evolution, or for models with masses that are low enough for radiative cores during the main sequence, $\mathcal{I}$ exhibits a wide spread based on the metallicity of the model (see Fig. 1). We note also that the variation in $\mathcal{I}$ with [Fe/H] decreases for increasing [Fe/H]. That is, the difference between tracks of [Fe/H] = –0.5 and 0 is larger than between tracks of [Fe/H] = 0 and +0.5 even though the difference in Z is much lower in the first case (as [Fe/H] scales logarithmically with Z).

To understand this, we compare models of the same mass and $\Delta\Pi_1$ but different metallicity in Fig. 3. The subsolar ([Fe/H] = –1) and supersolar ([Fe/H] = 0.5) models have lower values of max N^2 than the solar metallicity model. In the case of the subsolar model, the lower metallicity results in less efficient CNO burning, causing a broader shell burning region, and therefore, a lower μ gradient. For the supersolar model, the higher metallicity reduces the change in μ across the burning shell, also reducing the μ gradient. However, because the density of the subsolar model is higher than in the supersolar model, the value of N^3/ρ is significantly lower. Hence, the value of $\mathcal{I}$ is lowest for the model with subsolar metallicity. It may be confusing that the supersolar model has a higher value of $\mathcal{I}$ because the peak of N^3/ρ has a higher value in the solar metallicity model. However, the integrand in the numerator of Equation (4) is also weighted by $1/r^3$. Thus, the higher values of N^3/ρ in the bump below the burning-shell peak in the supersolar metallicity model lead to a slightly higher value of $\mathcal{I}$. The trend of a higher-metallicity model yielding a higher value of $\mathcal{I}$ at a given $\Delta\Pi_1$ value does not hold for all masses. Specifically, for higher-mass tracks, the balance between the μ gradient in the burning shell and the ρ profile differs, and the values of $\mathcal{I}$ are lower for the [Fe/H] = 0.5 models for than the [Fe/H] = 0.25 models. We conclude that the metallicity is an important parameter for determining accurate values of $\mathcal{I}$.

4. Finding best-fit models for determining $\mathcal{I}$

The models examined in Sect. 3 show that $\mathcal{I}$ is sensitive to several stellar properties, most notably, to the maximum extent of the main-sequence convective core and the metallicity. We now seek to assess the observational parameters that should be considered when using best-fit models to infer $\mathcal{I}$ for a given star. In addition, we also test two different approaches to choosing the input parameters of the grid of models used.

In order to make these assessments, we constructed a sample of 1000 synthetic stars taken from models in our Sobol grid. The sample was chosen to have a roughly uniform distribution in mass. For each synthetic star, we calculated the likelihood-weighted mean of $\mathcal{I}$ from each grid using the following sets of observed parameters:

Seismic:	$\Delta\nu, \Delta\Pi_1$
Seismic + Spectro:	$\Delta\nu, \Delta\Pi_1, T_{\rm eff}$, [Fe/H], $\sigma_{\rm [Fe/H]} = 0.25$
Seismic + HQ Spectro:	$\Delta\nu, \Delta\Pi_1, T_{\rm eff}$, [Fe/H], $\sigma_{\rm [Fe/H]} = 0.05$
Seismic + Surface:	$\Delta\nu, \Delta\Pi_1, T_{\rm eff}$, [Fe/H], $L, \sigma_{\rm [Fe/H]} = 0.05$.

For the seismic parameters $\Delta\nu$ and $\Delta\Pi_1$, we adopted the mean uncertainty reported in Hatt et al. (2024) of 0.01 μHz and 0.01 s, respectively. We assumed a 120 K uncertainty on our $T_{\rm eff}$ values (consistent with the values reported in Yu et al. 2018), and we let the uncertainty of the metallicity be either 0.25 dex (the mean value reported in Yu et al. 2018) or 0.05 dex (the adopted value of Pinsonneault et al. 2025). For the luminosity, we used an uncertainty of 2.25 $L_\odot$, which is 15% of the mean luminosity of our grid and corresponds to the typical uncertainty reported in Gaia DR2 (Andrae et al. 2018).

Although we constructed our grids with time steps roughly one-third of the MESA default values (by setting `time_delta_coeff = 0.3`), our time resolution is still not sufficiently high compared to the high precision of asteroseismic data. For example, the average change in $\Delta\Pi_1$ between successive models in our grids exceeds the observational uncertainty by ten times. Thus, when we restrict ourselves solely to the times where MESA calculated a model, we run the risk of skipping a model that fits the observations better. While it is possible to

decrease the MESA time step such that the change in observational parameters from one model to the next is below the observational uncertainties, this is extremely computationally intensive. Instead, as is common in the literature (e.g., Li et al. 2020; Huber et al. 2024; Grusnis et al. 2025), we opted to use interpolation to increase the effective time resolution of our grid. We interpolated our observed parameters and $\mathcal{I}$ values along each track onto a new time grid with steps of 10 000 years. For each synthetic star in our sample, we calculated a χ^2 value for each observable parameter P as

$$\chi^2_P = \frac{(P_{\rm obs} - P_{\rm model})^2}{\sigma^2_P}, \tag{6}$$

where $P_{\rm obs}$ refers to the value of our synthetic star, and $P_{\rm model}$ is the value from the models in our interpolated grid. We weighted all observables equally, and thus, the total χ^2 value for each set of observed parameters was a sum of the individual χ^2_P values. The inferred value of $\mathcal{I}_{\rm fit}$ for each synthetic star was found using

$$\mathcal{I}_{\rm fit} = \frac{\sum_{i=0}^{N_{\rm mod}} (\mathcal{L}_i \, \mathcal{I}_{i,\rm model})}{\sum_{i=0}^{N_{\rm mod}} \mathcal{L}_i}, \tag{7}$$

where $\mathcal{L}_i = \exp(-\chi^2_{i,\rm total}/2)$ is the likelihood of the ith model in the interpolated grid, and the sums were taken over all $N_{\rm mod}$ models in each interpolated grid. When we determined the value of $\mathcal{I}_{\rm fit}$ from the Sobol grid, we removed the track that contained the model used to generate our synthetic data.

For each synthetic star in our sample, we calculated the error between the known value of the global magnetic sensitivity ($\mathcal{I}_{\rm true}$) and the value found from the grid,

$$\frac{\delta\mathcal{I}}{\mathcal{I}} = \frac{\mathcal{I}_{\rm true} - \mathcal{I}_{\rm fit}}{\mathcal{I}_{\rm true}}. \tag{8}$$

For each set of observed parameters, we plot the distribution of $\delta\mathcal{I}/\mathcal{I}$ in Fig. 4 from each of our two grids. In all cases, the median on the distribution of the error in $\mathcal{I}$ is lower than 10%. However, there is a large change in the spread of our distributions (quantified by the first and third quartiles) depending on the grid and observational parameters used. For both grids, the spread of the errors is largest when only the seismic parameters are used. The median error and the spread of the errors are reduced when spectroscopic variables are included in the fit, although the linear grid is more sensitive to the precision of the metallicity measurement. In all cases, the global median error is similar between the two grids, but the spread is significantly smaller in our Sobol grid. We note that the typical uncertainty on $\Delta\Pi_1$ we chose based on Hatt et al. (2024) is much lower than in other works. We repeated our procedure assuming an uncertainty of 0.1 s on $\Delta\Pi_1$, which is the typical uncertainty of other works (e.g., Mosser et al. 2015; Vrard et al. 2016; Li et al. 2023a; Villate et al. 2026), and found that our results do not change.

To understand how $\delta\mathcal{I}/\mathcal{I}$ varies with stellar parameters, we show the median and the first and third quartiles of $\delta\mathcal{I}/\mathcal{I}$ for the seismic + spectro and seismic + HQ spectro distributions binned by the mass, [Fe/H], and $\Delta\Pi_1$ of the synthetic star in Fig. 5. The full distributions for the seismic + HQ results can be found in Appendix B. Figure 5 shows that high-precision metallicity values are essential to obtain $\mathcal{I}$ values for stars with low metallicity ([Fe/H] < -0.75), especially when using a less resolved grid, such as our Linear grid. The other important trend shown

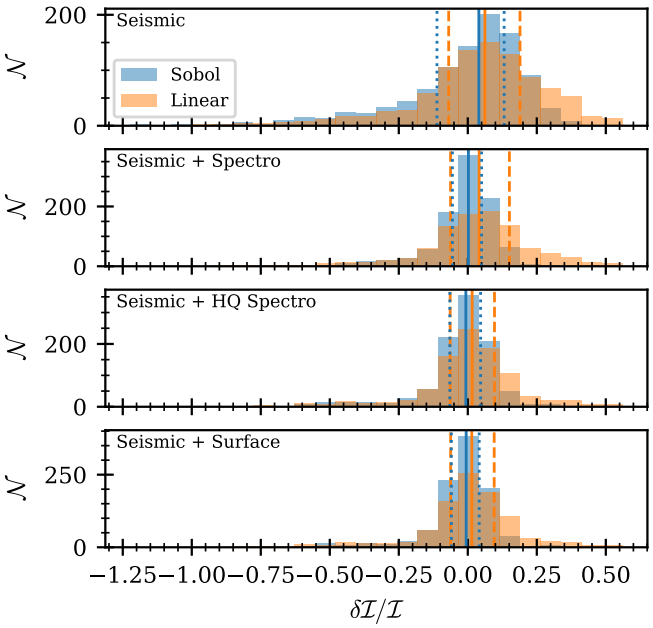


Fig. 4. Comparison of the error on our inferred value of $\mathcal{I}$ for different sets of observational parameters and grids. In each panel, we indicate the median of each grid distribution with a solid line and the first and third quartiles as dotted lines for the Sobol grid and dotted lines for the linear grid.

in Fig. 5 is that estimates of $\mathcal{I}$ become less certain for higher-mass stars, where the extent of the convective core during the main-sequence evolution becomes more important. Based on the results shown in Figs. 4 and 5, we consider a reasonable model-based uncertainty on $\mathcal{I}$ to be 10%, and we note that additional care should be taken when examining stars with low metallicity and higher masses. We note that increasing the resolution of the model grid by running more tracks would likely reduce this uncertainty even more. However, as we explore below, the dominant source of uncertainty in the magnetic field measurement in most cases remains the measurement of the frequency splittings and not $\mathcal{I}$ (see Eq. (3)), and we therefore did not consider the increased computational cost of running a larger grid to be necessary at this time.

5. Comparisons with previous work

We used our Sobol grid and fitting procedure to infer values of $\mathcal{I}$ for the stars studied by Li et al. (2023a) and Hatt et al. (2024). Figure 6 shows our values of $\mathcal{I}$ and those from previous works. Our primary purpose in these comparisons was to continue exploring differences in the modeling and fitting procedure, particularly in the comparison to the observational uncertainties of the measured magnetic splittings.

5.1. Comparison with Li et al. (2023a) $\mathcal{I}$ values

To determine our value of $\mathcal{I}$, we used the values of $T_{\rm eff}$, [Fe/H], $\Delta\nu$, and $\Delta\Pi_1$ reported by Li et al. (2023a). We used the radial modes returned by the GYRE oscillation code (Townsend & Teitler 2013) to calculate the $\Delta\nu$ values of our models, with more details provided in Appendix A. For the Li et al. (2023a) parameters with asymmetric uncertainties, we took symmetric uncertainties based on the higher of the two

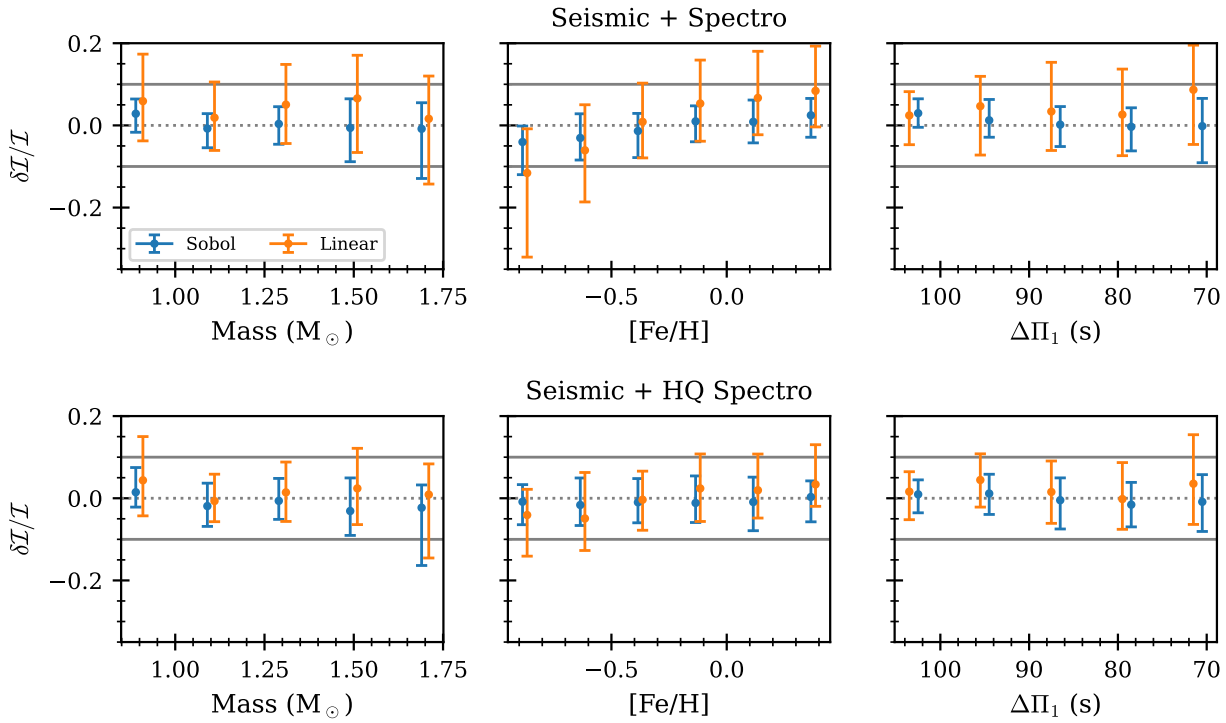


Fig. 5. Summary of $\delta\mathcal{I}/\mathcal{I}$ distributions calculated using the seismic + spectro (top) and seismic + HQ spectro (bottom) sets of parameters binned by mass (left), [Fe/H] (center), and $\Delta\Pi_1$ (right). Each bin is plotted at the center of the bin, with a slight offset for visibility. The points correspond to the median of the distribution, and the error bars indicate the first and third quartiles. The gray lines show errors of ±10%, which is our recommended value for the model-based uncertainty in $\mathcal{I}$ values determined from our Sobol grid using the seismic + HQ spectro set of observables.

values. Figure 6 shows that our values of $\mathcal{I}$ are consistent within our 10% uncertainty estimates for 7 of the 13 stars examined by Li et al. (2023a), and the remaining stars show differences close to 15%. Moreover, our $\mathcal{I}$ values are systematically higher than those obtained by Li et al. (2023a), and our value is lower for only one star. We attribute this bias to several factors. First, we did not use the individual mode frequencies and so did not correct our $\Delta\nu$ values for the surface term. By using uncorrected values of $\Delta\nu$ (which are typically higher than the corrected values), the model along a given track that matches the observed $\Delta\nu$ is more evolved than if we had applied a surface term correction, and it therefore exhibits a higher value of $\mathcal{I}$. The other important difference between the grids we used and the grid used by Li et al. (2023a) is the treatment of the opacity in the stellar atmosphere. This is important for determining the outer boundary condition used to solve the stellar structure equations and for the stellar atmosphere included when obtaining the oscillation frequencies. In our models, this opacity varies consistently with the local temperature and pressure. Li et al. (2023a) instead used a uniform opacity set by the opacity of the outermost cell in the structure model (for more details on this, we refer to Sect. 6 of Jermyn et al. 2023). Valle et al. (2025) have previously shown that this choice significantly changes the $f_{\Delta\nu}$ correction factor applied to the large frequency scaling relations.

To better understand the overall shift in $\mathcal{I}$ caused by these two choices, we constructed an additional set of synthetic stars from models with fixed atmosphere opacity values. Additionally, we applied the surface term prescription of Li et al. (2023b) and calculated $\Delta\nu$ values from the resulting frequencies[1]. We then used our Sobol grid to determine the best-fit value of $\mathcal{I}$ for this new set of synthetic stars. In contrast to the results presented in Sect. 4, our grid overestimates $\mathcal{I}$ by around 5% in the mass and $\Delta\Pi_1$ regimes covered by the Li et al. (2023a) sample. We conclude that the differences between our values of $\mathcal{I}$ and those of Li et al. (2023a) likely stem from our different treatment of the opacity in the stellar atmosphere and our use of $\Delta\nu$ values that were not corrected for the surface term. For future work, we recommend applying surface term corrections carefully and using models with a more realistic treatment of the atmospheric opacity.

5.2. Comparison with Hatt et al. (2024)

We focused on the stars with significant detections of magnetic splittings ($\delta\nu_{\rm mag} > 2\sigma_{\delta\nu_{\rm mag}}$) reported in Hatt et al. (2024). We used their reported values of $T_{\rm eff}$, [Fe/H], and $\Delta\Pi_1$. Instead of using their reported values of $\Delta\nu$, we used the radial mode frequencies directly. This allowed us to correct for the surface term using the two-term formulation of Ball & Gizon (2014), where the free parameters are determined independently for each model in our interpolated grid. We treated the frequencies as a single observable, that is,

$$\chi^2_{\rm freq} = \frac{1}{N_{\rm freq}} \sum_i^{N_{\rm freq}} \frac{(\nu_{i,\rm obs} - \nu_{i,\rm mod})^2}{\sigma^2_{\nu_i}}, \tag{9}$$

where $N_{\rm freq}$ is the number of frequencies, and $\nu_{i,\rm mod}$ is the model frequency after correcting for surface effects. Although not fully correct in a statistical sense, weighting a frequency χ^2 by the number of frequencies is common in the asteroseismic literature to avoid that the individual frequencies overwhelm any

[1] We did not apply this prescription when fitting the stars as the relation provided in Li et al. (2023b) was calibrated to a specific set of modeling choices that differ from ours.

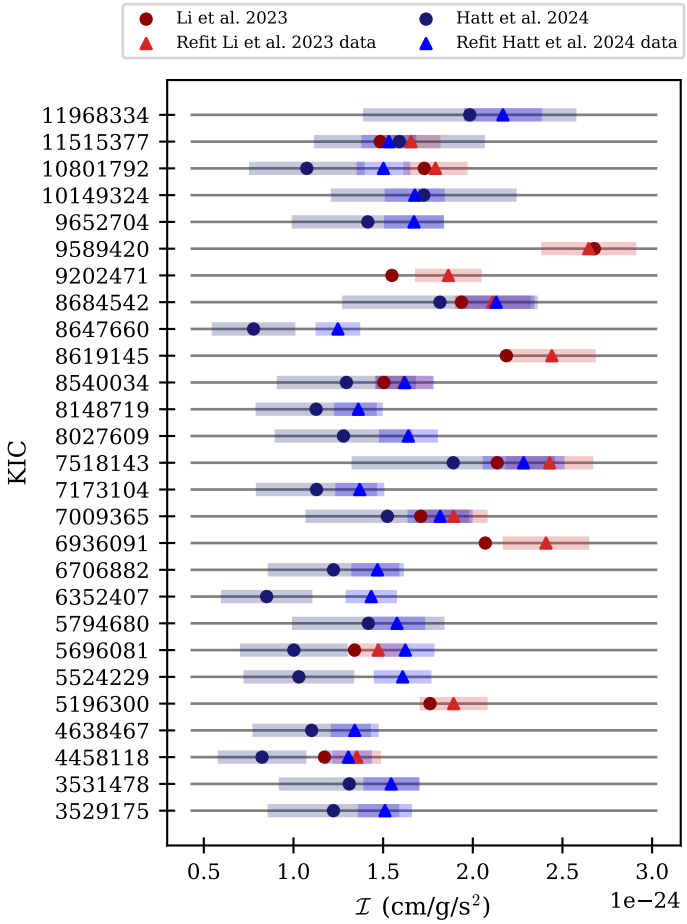


Fig. 6. Comparison between the values of $\mathcal{I}$ obtained using our grid and fitting method and the $\mathcal{I}$ values in previous works. There are several stars that were studied by Li et al. (2023a) and Hatt et al. (2024). As each study used different spectroscopic measurements and obtained different seismic parameters, we fit these stars twice, once using the stellar parameters from Li et al. (2023a) (plotted as red triangles), and the other time with the parameters from Hatt et al. (2024) (plotted as blue triangles). The shaded regions represent the uncertainties of $\mathcal{I}$ for our values and those of Hatt et al. (2024).

contribution from other global parameters (for a longer discussion of this topic, see Cunha et al. 2021).

When comparing our values of $\mathcal{I}$ to those obtained by Hatt et al. (2024), we again found that our values are systematically higher[2]. In addition, the differences between our values are larger, with an average difference of 20%. Although this is below the 30% uncertainty on $\mathcal{I}$ adopted by Hatt et al. (2024), it is larger than our adopted 10% uncertainties. Additionally, for six stars, our values of $\mathcal{I}$ differ from those in Hatt et al. (2024) by more than 40%.

The reasons for these large differences are less clear than the differences discussed in the previous section. Again, our choice to vary the opacity in the atmosphere likely played a role in pushing our results to higher values of $\mathcal{I}$. The difference in the grid construction might also play a role. Since we used our Sobol grid, $\alpha_{\rm mlt}$, $Y_{\rm init}$, and $f_{\rm ov}$ are free parameters. In the grid used by Hatt et al. (2024) , $\alpha_{\rm mlt}$ and $f_{\rm ov}$ were fixed and Y_i was varied linearly with $Z_{\rm init}$. Large differences in $\mathcal{I}$ are obtained for stars with masses low enough to have radiative cores on the main sequence, and the bias therefore cannot be fully explained by our variation in $f_{\rm ov}$. The treatments of $\alpha_{\rm mlt}$ and $Y_{\rm init}$ are known to change the stellar parameters inferred using seismic modeling (e.g., Li et al. 2024b), and it is perhaps to be expected that our different grid-construction techniques result in different values of $\mathcal{I}$. However, we were unable to find a satisfying explanation for why our choice to vary these parameters should yield systematically higher values of $\mathcal{I}$. However, for the stars analyzed by Li et al. (2023a) and Hatt et al. (2024), the values of $\mathcal{I}$ reported by Li et al. (2023a) are higher in all but one case. As the grid used by Li et al. (2023a) also varied $\alpha_{\rm mlt}$ and $Y_{\rm init}$, this supports the idea that the grid-construction technique can lead to systematically higher values of $\mathcal{I}$.

The final difference between our method and the methods of Li et al. (2023a) and Hatt et al. (2024) that is important to note, although it is difficult to predict its effect, is that we interpolated along the evolutionary tracks in our grid. This means that we were able to increase the effective time resolution of our grid without the additional computational expense of running MESA with smaller time steps. In theory, interpolation between tracks is also possible (increasing the resolution in the varied initial stellar and physical parameters), although we did not pursue this.

5.3. Comparison of radial magnetic field strength values and their uncertainties

Using the magnetic frequency shifts found by Li et al. (2023a) and Hatt et al. (2024), we calculated the resulting average magnetic field strengths using our values of $\mathcal{I}$ according to Equation (3). Figure 7 compares our results to those of the previous works. The higher values of $\mathcal{I}$ we found mean that our magnetic field strengths are generally lower than in previous works. As we did not correct for surface effects when fitting the stars in Li et al. (2023a), our values should not be taken as corrections to the previous values, and so we do not provide them. In the case of the sample of Hatt et al. (2024), we were able to correct for surface effects, and so we provide our new values in Table 1. Although our values of $\mathcal{I}$ differ, the final field strength values agree within the final uncertainties for all of the stars in Li et al. (2023a) and Hatt et al. (2024). This is expected because for most of the stars, the uncertainty in the final result is dominated by the uncertainty in the measured magnetic shift. The percent uncertainty in the magnetic splitting for four stars in the Hatt et al. (2024) sample is below 10%. For these four stars, the model-based uncertainty of $\mathcal{I}$ is larger than the uncertainty on the average magnetic field strength. This shows that although most measurements are not yet precise enough for the stellar modeling to be the dominant source of uncertainty, in stars with the most precisely measured magnetic shifts, the modeling choices used to obtain $\mathcal{I}$ can be significant.

6. Conclusions

We used stellar models to explore the global magnetic sensitivity, $\mathcal{I}$, which is used to infer internal magnetic field strengths in red giants. We studied the variation in $\mathcal{I}$ with stellar parameters and determined how well $\mathcal{I}$ can be recovered using grid-based techniques and different observational constraints. We found that the mass dependence of $\mathcal{I}$ is strongest for models where the hydrogen burning shell is still below the mean molecular weight

[2] In addition, we found one star (KIC 9508757) where our method did not return a value of $\mathcal{I}$ because this star is below the $\Delta\nu - \Delta\Pi_1$ sequence expected from single-star evolution. This suggests that KIC 9508757 might be the product of binary interactions (Deheuvels et al. 2022). As we did not account for these effects, we did not include this star in our comparisons.

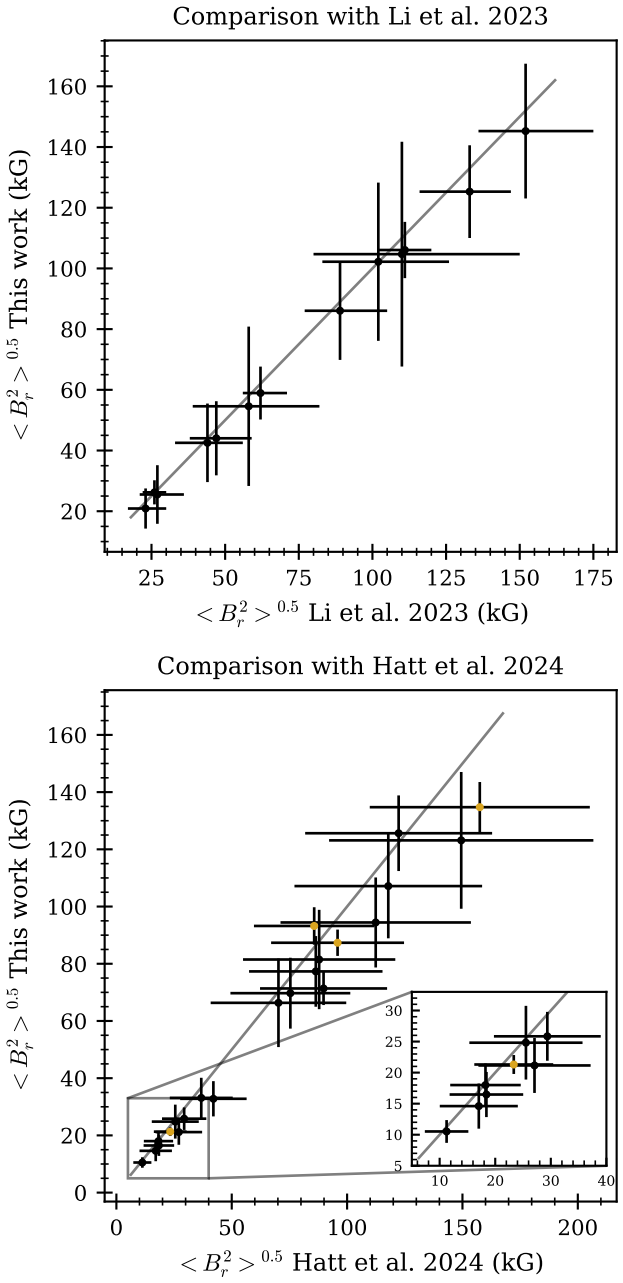


Fig. 7. Comparison of our inferred average magnetic field strengths with those of previous studies. In both panels, we plot the 1:1 line in gray. In the lower panel, the yellow points indicate stars for which our model-based uncertainty of $\mathcal{I}$ is larger than the uncertainty on the observed magnetic splittings.

gradient caused by the recession of the convective core during the main-sequence evolution. After this point, or in models with radiative cores on the main sequence, the value of $\mathcal{I}$ depends more on the metallicity than on the mass.

To test how accurately $\mathcal{I}$ can be determined from observed parameters, we constructed a set of synthetic stars and attempted to infer $\mathcal{I}$ from our model grids. We tested several different sets of observed parameters and found that for all sets, the median error on $\mathcal{I}$ is smaller than 5%, with spreads between 10% and 15%. We obtained the best results when our fitting procedure included high-quality spectroscopic data, particularly [Fe/H] values, in addition to the global seismic parameters $\Delta\nu$ and $\Delta\Pi_1$. Based on our tests, we recommended adopting a 10% uncertainty on $\mathcal{I}$ when found using this method.

Table 1. Global magnetic sensitivities and average radial magnetic field strengths obtained from our procedure for stars in Hatt et al. (2024).

KIC	$\mathcal{I}$ (10^{-24} cm/g/s^2)	$\langle B_r^2 \rangle^{0.5}$ (kG)
3529175	1.489 ± 0.149	107.2 ± 18.3
3531478	1.532 ± 0.153	69.7 ± 12.4
4458118	1.292 ± 0.129	94.4 ± 15.7
4638467	1.338 ± 0.134	81.5 ± 17.4
5524229	1.721 ± 0.172	21.2 ± 4.4
5696081	1.359 ± 0.136	134.7 ± 8.8
5794680	1.614 ± 0.161	24.8 ± 5.9
6352407	1.358 ± 0.136	32.8 ± 6.2
6706882	1.251 ± 0.125	125.6 ± 13.2
7009365	1.836 ± 0.184	77.3 ± 12.4
7173104	1.488 ± 0.149	33.1 ± 7.0
7518143	2.28 ± 0.228	21.3 ± 1.5
8027609	1.622 ± 0.162	66.3 ± 15.5
8148719	1.649 ± 0.165	14.6 ± 3.6
8540034	1.627 ± 0.163	25.8 ± 3.9
8647660	1.246 ± 0.125	123.1 ± 23.9
8684542	2.187 ± 0.219	87.3 ± 4.6
9652704	1.794 ± 0.179	16.5 ± 3.6
10149324	1.791 ± 0.179	18.0 ± 3.5
10801792	1.696 ± 0.17	71.4 ± 5.8
11515377	1.355 ± 0.136	93.2 ± 6.5
11968334	2.289 ± 0.229	10.5 ± 1.8

In comparison to previously reported values of $\mathcal{I}$, our procedure yields systematically higher values of $\mathcal{I}$. In the case of the stars studied by Li et al. (2023a), we attribute this primarily to a difference in the treatment of atmospheric opacity in our models and our use of model $\Delta\nu$ values without applying a surface term correction. We attribute the large differences in $\mathcal{I}$ between this work and Hatt et al. (2024) to our differing grid-construction approaches, notably the treatment of the mixing length and overshoot parameters and the initial helium abundance. We note that while we focused on red giant stars, a similar approach has been proposed to measure internal magnetic fields in main-sequence f-type stars (Takata et al. 2026). Our results suggest that it may be important to account for model-based uncertainties in these stars as well.

One important limitation of this work is that we only examined single-star evolution. Some stars with measured magnetic splittings show evidence of binary interactions (Deheuvels et al. 2022; Villate et al. 2026). These interactions are known to change the internal structure of the star (Rui & Fuller 2021), and hence, the value of $\mathcal{I}$ (see Muntean et al., in prep.). For stars where single star evolution is appropriate, however, our grid and fitting method provide reliable estimates of $\mathcal{I}$ with uncertainties below the uncertainty of typical observations.

Data availability

To aid future measurements of internal magnetic fields in red giants, we provide both our Sobol grid and our scripts to infer values of $\mathcal{I}$ at `https://zenodo.org/records/21032697`.

Acknowledgements. L. Buchele and L. Bugnet gratefully acknowledge support from the European Research Council (ERC) under the Horizon Europe pro-

gramme (Calcifer; PI Bugnet; Starting Grant agreement N°101165631). While partially funded by the European Union, views and opinions expressed are, however, those of the authors only and do not necessarily reflect those of the European Union or the European Research Council. Neither the European Union nor the granting authority can be held responsible for them.

References

Ahlborn, F., Bellinger, E. P., Hekker, S., Basu, S., & Mokrytska, D. 2022, A&A, 668, A98
Ahlborn, F., Bellinger, E. P., Hekker, S., Basu, S., & Mokrytska, D. 2025, A&A, 693, A274
Andrae, R., Fouesneau, M., Creevey, O., et al. 2018, A&A, 616, A8
Angulo, C., Arnould, M., Rayet, M., et al. 1999, Nucl. Phys. A, 656, 3
Ball, W. H., & Gizon, L. 2014, A&A, 568, A123
Beck, P. G., Montalban, J., Kallinger, T., et al. 2012, Nature, 481, 55
Bellinger, E. P., Angelou, G. C., Hekker, S., et al. 2016, ApJ, 830, 31
Bhattacharya, S., Das, S. B., Bugnet, L., Panda, S., & Hanasoge, S. M. 2024, ApJ, 970, 42
Buchele, L. 2025, Res. Notes AAS, 9, 193
Bugnet, L. 2022, A&A, 667, A68
Bugnet, L., Prat, V., Mathis, S., et al. 2021, A&A, 650, A53
Cantiello, M., Mankovich, C., Bildsten, L., Christensen-Dalsgaard, J., & Paxton, B. 2014, ApJ, 788, 93
Ceillier, T., Tayar, J., Mathur, S., et al. 2017, A&A, 605, A111
Cunha, M. S., Roxburgh, I. W., Aguirre Børsen-Koch, V., et al. 2021, MNRAS, 508, 5864
Cyburt, R. H., Amthor, A. M., Ferguson, R., et al. 2010, ApJS, 189, 240
Das, S. B., Einramhof, L., & Bugnet, L. 2024, A&A, 690, A217
Deheuvels, S., Doğan, G., Goupil, M. J., et al. 2014, A&A, 564, A27
Deheuvels, S., Ballot, J., Gehan, C., & Mosser, B. 2022, A&A, 659, A106
Deheuvels, S., Li, G., Ballot, J., & Lignières, F. 2023, A&A, 670, L16
Deheuvels, S., Ballot, J., Lignières, F., Li, G., & Villate, M. 2026, A&A, 709, A224
Dhouib, H., Mathis, S., Bugnet, L., Van Reeth, T., & Aerts, C. 2022, A&A, 661, A133
Di Mauro, M. P., Ventura, R., Cardini, D., et al. 2016, ApJ, 817, 65
Eggenberger, P., den Hartogh, J. W., Buldgen, G., et al. 2019, A&A, 631, L6
Eggenberger, P., Moyano, F. D., & den Hartogh, J. W. 2022, A&A, 664, L16
Farag, E., Fontes, C. J., Timmes, F. X., et al. 2024, ApJ, 968, 56
Ferguson, J. W., Alexander, D. R., Allard, F., et al. 2005, ApJ, 623, 585
Fuller, G. M., Fowler, W. A., & Newman, M. J. 1985, ApJ, 293, 1
Fuller, J., Cantiello, M., Stello, D., Garcia, R. A., & Bildsten, L. 2015, Science, 350, 423
Fuller, J., Piro, A. L., & Jermyn, A. S. 2019, MNRAS, 485, 3661
Gehan, C., Mosser, B., Michel, E., Samadi, R., & Kallinger, T. 2018, A&A, 616, A24
Gouhier, B., Jouve, L., & Lignières, F. 2022, A&A, 661, A119
Grevesse, N., & Sauval, A. J. 1998, Space Sci. Rev., 85, 161
Grusnis, S., Tayar, J., & Godoy-Rivera, D. 2025, ApJ, 993, 96
Hatt, E. J., Ong, J. M. J., Nielsen, M. B., et al. 2024, MNRAS, 534, 1060
Henyey, L., Vardya, M. S., & Bodenheimer, P. 1965, ApJ, 142, 841
Herwig, F. 2000, A&A, 360, 952
Huber, D., Slumstrup, D., Hon, M., et al. 2024, ApJ, 975, 19
Iglesias, C. A., & Rogers, F. J. 1993, ApJ, 412, 752
Iglesias, C. A., & Rogers, F. J. 1996, ApJ, 464, 943
Irwin, A. W. 2004, The FreeEOS Code for Calculating the Equation of State for Stellar Interiors, http://freeeos.sourceforge.net/
Jermyn, A. S., Schwab, J., Bauer, E., Timmes, F. X., & Potekhin, A. Y. 2021, ApJ, 913, 72
Jermyn, A. S., Bauer, E. B., Schwab, J., et al. 2023, ApJS, 265, 15
Langanke, K., & Martínez-Pinedo, G. 2000, Nucl. Phys. A, 673, 481
Li, Y., & Joyce, M. 2025, ApJ, 994, 127
Li, T., Bedding, T. R., Christensen-Dalsgaard, J., et al. 2020, MNRAS, 495, 3431
Li, G., Deheuvels, S., Ballot, J., & Lignières, F. 2022a, Nature, 610, 43
Li, T., Li, Y., Bi, S., et al. 2022b, ApJ, 927, 167
Li, G., Deheuvels, S., Li, T., Ballot, J., & Lignières, F. 2023a, A&A, 680, A26
Li, Y., Bedding, T. R., Stello, D., et al. 2023b, MNRAS, 523, 916
Li, G., Deheuvels, S., & Ballot, J. 2024a, A&A, 688, A184
Li, Y., Bedding, T. R., Huber, D., et al. 2024b, ApJ, 974, 77
Lignières, F., Ballot, J., Deheuvels, S., & Galoy, M. 2024, A&A, 683, A2
Loi, S. T. 2020, MNRAS, 496, 3829
Mathis, S., & Bugnet, L. 2023, A&A, 676, L9
Mathis, S., Bugnet, L., Prat, V., et al. 2021, A&A, 647, A122
Meduri, D. G., Jouve, L., & Lignières, F. 2024, A&A, 683, A12
Mosser, B., Elsworth, Y., Hekker, S., et al. 2012a, A&A, 537, A30
Mosser, B., Goupil, M. J., Belkacem, K., et al. 2012b, A&A, 548, A10
Mosser, B., Vrard, M., Belkacem, K., Deheuvels, S., & Goupil, M. J. 2015, A&A, 584, A50
Moyano, F. D., Eggenberger, P., Mosser, B., & Spada, F. 2023, A&A, 673, A110
Oda, T., Hino, M., Muto, K., Takahara, M., & Sato, K. 1994, At. Data Nucl. Data Tables, 56, 231
Paxton, B., Bildsten, L., Dotter, A., et al. 2011, ApJS, 192, 3
Paxton, B., Cantiello, M., Arras, P., et al. 2013, ApJS, 208, 4
Paxton, B., Marchant, P., Schwab, J., et al. 2015, ApJS, 220, 15
Paxton, B., Schwab, J., Bauer, E. B., et al. 2018, ApJS, 234, 34
Paxton, B., Smolec, R., Schwab, J., et al. 2019, ApJS, 243, 10
Pinsonneault, M. H., Zinn, J. C., Tayar, J., et al. 2025, ApJS, 276, 69
Rogers, F. J., & Nayfonov, A. 2002, ApJ, 576, 1064
Rui, N. Z., & Fuller, J. 2021, MNRAS, 508, 1618
Rui, N. Z., Ong, J. M. J., & Mathis, S. 2024, MNRAS, 527, 6346
Sobol', I. 1967, USSR Comput. Math. Math. Phys., 7, 86
Spada, F., Gellert, M., Arlt, R., & Deheuvels, S. 2016, A&A, 589, A23
Takahashi, K., & Langer, N. 2021, A&A, 646, A19
Takata, M., Murphy, S. J., Kurtz, D. W., Saio, H., & Shibahashi, H. 2026, MNRAS, 545, staf2153
Townsend, R. H. D., & Teitler, S. A. 2013, MNRAS, 435, 3406
Triana, S. A., Corsaro, E., De Ridder, J., et al. 2017, A&A, 602, A62
Valle, G., Dell'Omodarme, M., Prada Moroni, P. G., & Degl'Innocenti, S. 2025, A&A, 698, A111
Villate, M., Deheuvels, S., & Ballot, J. 2026, A&A, 707, A366
Vrard, M., Mosser, B., & Samadi, R. 2016, A&A, 588, A87
Yu, J., Huber, D., Bedding, T. R., et al. 2018, ApJS, 236, 42

Appendix A: Details of MESA calculations

Here we provide more details about our MESA setup, including the model physics we kept constant between our two grids and our calculation of the asteroseismic parameters. We provide the MESA and GYRE inlists we used and our `run_star_extras` files at the Zendo link provided above.

A.1. Model physics

As noted in the main text, most of our physics choices follow those in Li & Joyce (2025). We use the default blend of equation of state data from OPAL (Rogers & Nayfonov 2002), FreeEOS (Irwin 2004), and Skye (Jermyn et al. 2021). We use the solar abundance scale of Grevesse & Sauval (1998) to scale the initial metal abundances of our models and also when calculating their [Fe/H] values. Our radiative opacity values are taken from OPAL (Iglesias & Rogers 1993, 1996) and supplemented in the low-temperature regime by values from Ferguson et al. (2005). We adopt the cubic interpolation scheme for our opacity values described in Farag et al. (2024). Our nuclear network choice is `pp_cno_extras_o18_ne22.net` with reaction rates taken from JINA REACLIB (Cyburt et al. 2010), NACRE (Angulo et al. 1999), and additional tabulated weak reaction rates (Fuller et al. 1985; Oda et al. 1994; Langanke & Martínez-Pinedo 2000).

We use the mixing length formulation of Henyey et al. (1965). We determine convective boundaries using the Ledoux criterion and turn on MESA's convective premixing scheme (Paxton et al. 2019). Although the adopted value of the overshooting parameter varies between our models, all models use exponential overshooting (Herwig 2000) with $f_0 = 0.004$. We follow the recommendation of Buchele (2025) and set `overshoot_D_min` to 10^{-2} cm^2/s. In addition, we implement a routine to ensure that extra mesh points are placed around the overshooting regions. For our atmospheric boundary conditions, we adopt the Eddington T-τ relation with a varying opacity consistent with the local temperature and pressure, except during pre-main-sequence evolution, where adopting a fixed opacity improved the stability of the models.

A.2. Calculation of asteroseismic parameters

Since there are several ways of obtaining seismic parameters from stellar models, we provide the details of our calculations here.

A.2.1. $\Delta\nu$

To obtain a value of $\Delta\nu$ for each model in our grid, we calculate the radial mode frequencies using GYRE (Townsend & Teitler 2013). We obtain frequencies in the range 0.001μHz to $2\nu_{ac}$ where ν_{ac} is the acoustic cutoff frequency of the model. Defining the frequency range in this manner allows us to call GYRE on-the-fly as MESA is running rather than as a post-processing step. However, this range of frequencies is far larger than what is observed in these stars. To account for this, we calculate $\Delta\nu$ using a weighted least squares fit between the frequencies and their radial orders. Our weighting function is a Gaussian centered at $\nu_{\max}$ with a FWHM of $0.66\nu_{\max}^{0.88}$, which is the scaling of red giant oscillation power excess found by Mosser et al. (2012a).

A.2.2. $\Delta\Pi_1$ and $\mathcal{I}$

Although we use GYRE to calculate the radial mode frequencies, calculating mixed modes is significantly more computationally expensive, and so we opt to use the asymptotic form of $\Delta\Pi_1$ given in Equation 5. While this is a quantity that MESA can provide, we find that the values of $\Delta\Pi_1$ outputted by the default routine do not evolve smoothly along a given track. Instead, there are points where the value jumps abruptly from one model to the next, see the top panel of Fig. A.1. This occurs because the integration limits are defined by N^2 crossing $(2\pi\nu_{\max})^2$; however, there is no guarantee that MESA places a mesh point at the exact point where this crossing occurs. Thus, $\Delta\Pi_1$ jumps when the integration limits of Equation 5 are expanded by one zone. Although we show this for only for the inner turning point in the lower two panels of Fig. A.1, we find similar issues (of smaller magnitude) at the outer turning point. These numerical issues cause $\Delta\Pi_1$ to be slightly overestimated for a period leading up to the jump and also introduce significant interpolation error, shown in the second panel of Fig. A.1. To resolve this issue, we interpolate N^2 around both the inner and outer turning points to find the exact radius where $N^2 = (2\pi\nu_{\max})^2$. We then include

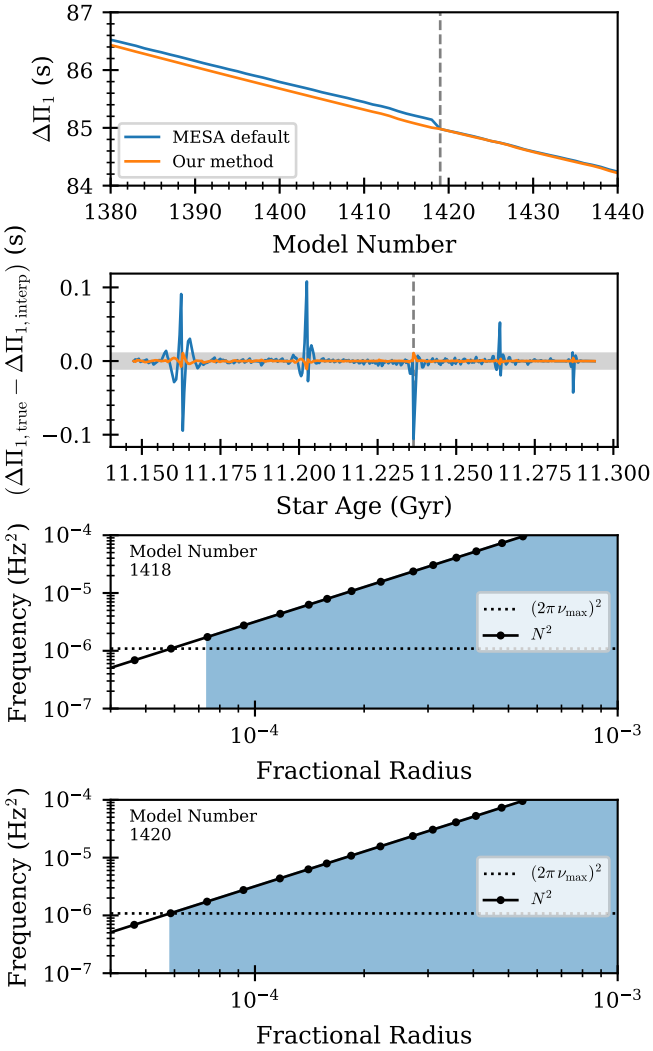


Fig. A.1. Comparison of the MESA default way of calculating $\Delta\Pi_1$ and our method. The top panel shows the evolution of $\Delta\Pi_1$ calculated with each method. The second panel shows the interpolation error from each method, with the gray shaded region indicating the average uncertainty of $\Delta\Pi_1$ reported in Hatt et al. (2024). The bottom two panels show, in the blue areas, the region used by MESA to calculate $\Delta\Pi_1$ for two models on either side of the jump indicated by the dashed vertical line in the top two panels.

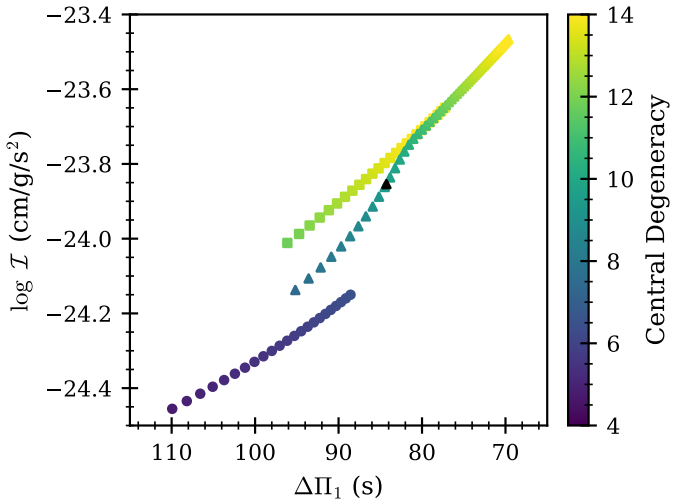


Fig. B.1. Change in central electron degeneracy (described as the Fermi energy in units of k_bT) for three different solar metallicity tracks from our Linear grid. The marker indicates the mass: 1M$_\odot$ (square), 1.55M$_\odot$ (triangle), 1.6M$_\odot$ (circle). The black triangle indicates the point where the 1.55M$_\odot$ track joins the degenerate sequence in the $\Delta\nu$ – $\Delta\Pi_1$ diagram.

these partial zones in our calculation of $\Delta\Pi_1$. This procedure is also applied to the integrals used to calculate $\mathcal{I}$, see Equation 4.

Appendix B: Additional figures

Here we provide a few additional figures for the interested reader. In Fig. B.1, we show how the central electron degeneracy changes for several solar metallicity tracks of various masses. In Figs. B.3, B.2, and B.4, we provide the full distributions of $\delta\mathcal{I}/\mathcal{I}$ found when fitting using the Seismo + HQ Spectro observables binned by mass, [Fe/H], and $\Delta\Pi_1$ that were summarized in Fig. 5.

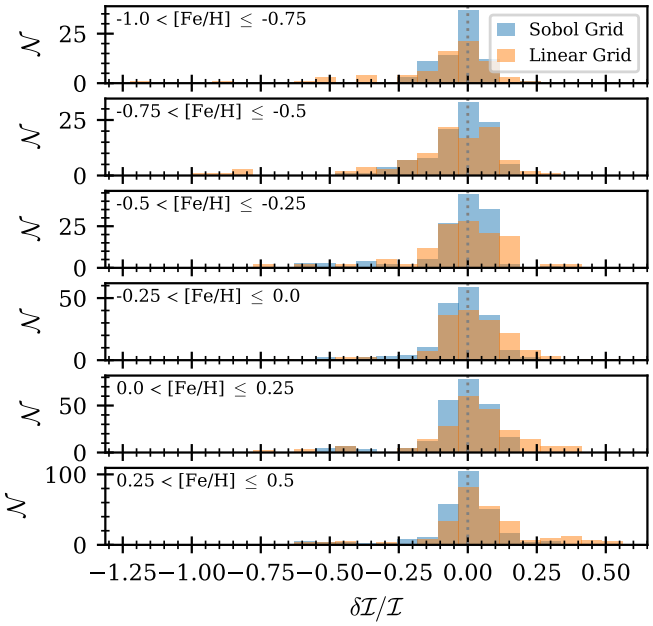


Fig. B.2. Comparison of the results best fit models found using seismic + HQ spectro variables for different values of the synthetic star's [Fe/H].

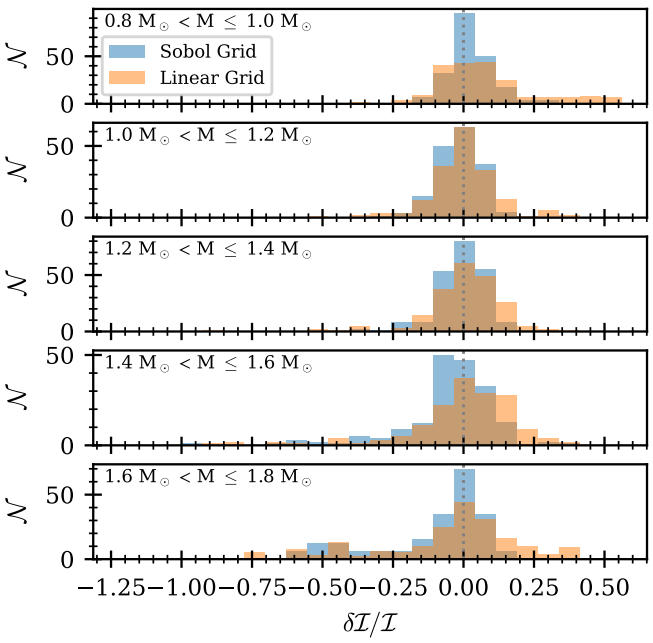


Fig. B.3. Comparison of the results best fit models found using seismic + HQ spectro variables for different values of the synthetic star's mass.

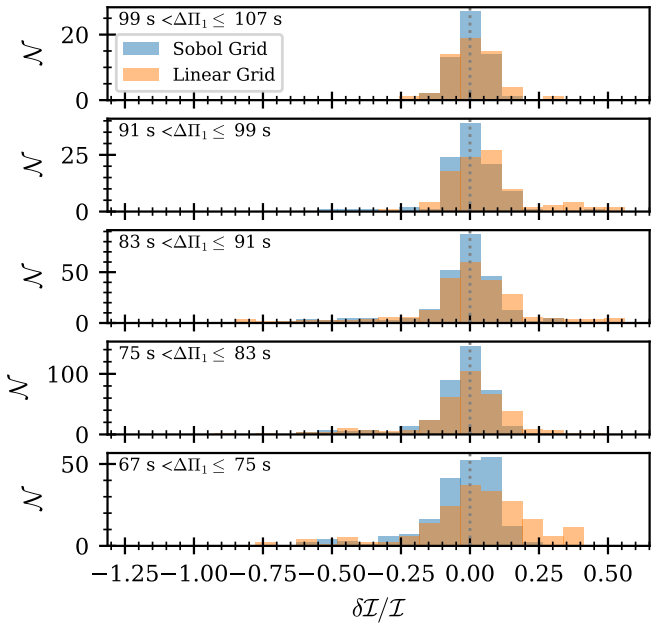


Fig. B.4. Comparison of the results best fit models found using seismic + HQ spectro variables for different values of the synthetic star's $\Delta\Pi_1$.